



JGR Space Physics

RESEARCH ARTICLE

10.1029/2024JA032557

Key Points:

- Cluster observed suprathermal outflowing H⁺ ion beams and ion conics in the lobe after the impact of an interplanetary (IP) shock
- The outflowing H⁺ ions appeared
 ~10 min after the shock impact and
 ~8 min after enhanced downward DC
 Poynting fluxes
- The suprathermal outflowing H⁺ ions were likely pre-existing thermal polar wind being accelerated caused by the enhanced Poynting fluxes

Supporting Information:

Supporting Information may be found in the online version of this article.

Correspondence to:

C.-P. Wang, cat@atmos.ucla.edu

Citation:

Wang, C.-P., Mouikis, C. G., Wang, X., Masson, A., & Lin, Y. (2024). Suprathermal outflowing H⁺ ions in the lobe driven by an interplanetary shock: 1. An observation event. *Journal of Geophysical Research: Space Physics*, 129, e2024JA032557. https://doi.org/10.1029/2024JA032557

Received 16 FEB 2024 Accepted 29 JUN 2024

© 2024. American Geophysical Union. All Rights Reserved.

Suprathermal Outflowing H⁺ Ions in the Lobe Driven by an Interplanetary Shock: 1. An Observation Event

Chih-Ping Wang¹, C. G. Mouikis², Xueyi Wang³, Arnaud Masson⁴, and Yu Lin³

¹Department of Atmospheric and Oceanic Sciences, University of California, Los Angeles, Los Angeles, CA, USA, ²Space Science Center, University of New Hampshire, Durham, NH, USA, ³Physics Department, Auburn University, Auburn, AL, USA, ⁴European Space Agency, European Space Astronomy Center, Madrid, Spain

Abstract To better understand how sharp changes in the solar wind and interplanetary magnetic field conditions affect the ionosphere outflows at high latitudes, we analyze an event observed on 17 July 2002 showing suprathermal (tens to hundreds of eV) outflowing H⁺ ions in the lobe driven by the impact of an interplanetary (IP) shock. A spacecraft in the lobe at altitudes of $\sim 6.5 R_E$ first observed enhanced downward DC Poynting fluxes ~ 2 min after the shock impact and then, another 8 min later, the appearance of suprathermal outflowing H⁺ ions as ion beams and ion conics. The increasing downward DC Poynting fluxes and the increasing outflowing H⁺ fluxes that appeared later were highly correlated because they shared a similar increasing trend with a time scale of ~ 5 min. To explain such time delay and correlation, we conclude that a plausible scenario was that the enhanced DC Poynting fluxes reached down to lower altitudes, drove processes to accelerate the pre-existing polar wind ions to ion beams and ion conics, and then these newly generated suprathermal ions flowed upward to the spacecraft altitudes. This event indicates that an IP shock can drive a significant amount of suprathermal H⁺ outflows from the polar cap.

1. Introduction

Solar wind ions and the outflow ions from the ionosphere are the two ion sources for the Earth's magnetosphere (e.g., Chappell et al., 1987, 2000; Kistler et al., 2023). The main outflow ion species are H⁺, H_e⁺, and O⁺ ions. The outflow ions can come out of the ionosphere at different latitudes and flow into different magnetosphere regions, including the cusp, mantle, and lobe at high latitudes within the open field-line region and the plasma sheet and plasmasphere at lower latitudes within the closed field-line region. The lobe outflow ions are subsequently transported tailward, and some of them can later enter the tail current sheet and drift earthward, contributing to the plasma sheet and ring current populations (e.g., Kistler et al., 2010; Mouikis et al., 2010). Complicated multi-step processes are involved in generating ionospheric ion outflows. For example, upwelling O^+ ions interacting with the H neutrals create H^+ ions through charge exchange $(O^+ + H \rightarrow H^+ + O)$, which provides the source ions for the H⁺ outflow. These source ions are then accelerated by different mechanisms to become ion outflows, which, based on the ion energies, can be separated into two categories (e.g., Yau et al., 2011): (a) "bulk ion flows" are thermal outflows with energies up to a few eV, such as the polar wind (e.g., Yau et al., 2007), and (b) "suprathermal ion outflows" are more energetic outflows with energies from tens to hundreds of eV, such as ion beams (the maximum particle flux is peaked along the upward magnetic field direction) and ion conics (the maximum particle flux is peaked at an angle to the magnetic field) (e.g., Horwitz et al., 1982; Sharp et al., 1977). Past studies identified six outflow drivers (e.g., Strangeway et al., 2000, 2005; Zhao et al., 2020), including downward DC Poynting flux (note that downward is toward the ionosphere in this paper), downward AC Poynting flux, electric field amplitude of extremely low-frequency waves, precipitating electron density, precipitating electron number flux; and precipitating electron energy flux. These drivers can contribute to ion outflows through various processes at different altitudes from the ionosphere up to a few R_E . These processes can result in an increased number of upwelling ions below ~1,000 km, and polar wind ions, ion beams, and ion conics above 1,000 km. The intensities of these outflow drivers depend on the external coupling of the magnetosphere with the solar wind as well as the internal disturbances within the magnetosphere. An interplanetary (IP) shock is considered an important solar wind driving condition because the associated changes in the interplanetary magnetic field (IMF) and the solar wind dynamic pressure (P_{SW}) are sharp and large and the impact of P_{SW} on the magnetosphere is global and rather immediate. Observations showed that P_{SW} disturbances can enhance polar wind particle fluxes above the polar cap (e.g., Moore et al., 1999).

WANG ET AL. 1 of 18

Using observations at ~6,000 km altitude during the solar minimum and non-storm conditions, Peterson et al. (2008) showed statistically that suprathermal outflows are much less frequently observed above the polar cap, as compared to the polar wind. In this study, we investigate an event showing an IP shock can drive a significant amount of suprathermal H⁺ outflows from the polar cap. A Cluster spacecraft, in the lobe at altitudes of $\sim 6 R_E$ above the polar cap, observed the appearance of suprathermal outflowing H⁺ ions ~ 10 min after the shock impact, and ~8 min after observing enhanced downward DC Poynting fluxes. The outflowing ions had energies from ~20 to 2,000 eV and the pitch-angle features of ion beams and ion conics. The initial increase in the outflow fluxes was well correlated with the initial increase in the downward DC Poynting fluxes with the 8-min time delay. A plausible scenario to explain such observations is the acceleration of pre-existing H⁺ polar wind ions at low altitudes over the polar cap by processes driven by the enhanced Poynting fluxes and the subsequent upward transport of these suprathermal ions to the Cluster altitudes at \sim 6 R_E . In a companion paper (Wang et al., 2024; hereafter referred to as Paper 2), we simulate H⁺ ions coming from both the solar wind and ionosphere sources using a 3D global hybrid code and present the simulation-observation comparison results to support our explanation of the Cluster observations. In this paper, Cluster data are described in Section 2. We present the details of the event and our analysis in Section 3 and discuss the scenario in Section 4. We summarize our findings in Section 5.

2. Data

For the event presented in this paper, we use observations from Cluster (Escoubet et al., 1997). DC magnetic field measurements are provided by the FluxGate Magnetometer (FGM, Balogh et al., 1997), the DC electric fields by the Electric Drift Instrument (EDI, Paschmann et al., 1997), the AC electric field fluctuations by the Spatio-Temporal Analysis of Field Fluctuations (STAFF, Cornilleau-Wehrlin et al., 2003) instrument, the H⁺ ions from ~40 eV to 40 keV by the Cluster Ion Spectrometry/Composition and Distribution Function analyser (CIS/ CODIF, Rème et al., 2001) instrument, and the electrons from 0.59 eV to 26.4 keV by Plasma Electron and Current Experiment (PEACE, Johnstone et al., 1997) instrument. Cluster mission consists of four spacecraft (C1-C4) launched in 2000, in a nominal 4 $R_E \times 19 R_E$ polar orbit. During this event, C2 was close to C1 (~1 R_E apart) while C4 was closer to C3 (\sim 0.6 R_E apart) (See Figures S1a and S1b in Supporting Information S1). The four spacecraft crossed the cusp in the southern hemisphere successively like a "string of pearls" with C1 and C2 reaching the cusp about 60 min earlier than C3 and C4 (C1 and C3 were $\sim 2.4 R_E$ apart). For this study, we use the data from C1 and C3 because the CIS/CODIF measurements were not available for C2. The ions observed by C3 and C4 were very similar (see Figures S1f and S1h in Supporting Information S1) but the EDI measurements were only available for C3 during the event. The 1-min solar wind and IMF data and the SYM-H index are from OMNI. Note that the OMNI solar wind and IMF data have been propagated from the spacecraft locations in the upstream solar wind to the bow shock nose (Papitashvili & King, 2020). The SYM-H index can be used as a high-resolution Dst index (Wanliss & Showalter, 2006). The PC(N) index is the Polar Cap definitive Index determined from the North polar cap station (Qaanaaq, +85° magnetic latitude) in Greenland (World Data Center For Geomagnetism, Copenhagen (2019)). Note no other observations from the ground, such as radar measurements of the ionosphere convection, and low-altitude satellites were available near the footprints of Cluster during this event.

3. Event Observation

3.1. Event Overview

We investigate an IP shock event on 17 July 2002 when one of the Cluster spacecraft was in the cusp while another was in the lobe not far from the cusp. The changes in the IMF and solar wind parameters associated with the IP shock are shown in Figures 1a–1e. The $P_{\rm SW}$ jump was very sharp with an increase from 2 to 10 nPa within 1 min (Figure 1e). The impact time of the $P_{\rm SW}$ jump on the magnetosphere was ~16:02 UT (the vertical dotted line), as indicated by a sharp jump in SYM-H (Figure 1f). SYM-H first increased quickly from -17 to 24 nT within ~5 min and then gradually decreased to ~7 nT. This transient response with an initial quick increase within 5 min followed by a decrease was also seen in the electric and magnetic fields and the associated downward DC Poynting fluxes observed in the lobe, as presented in Section 3.5, and outflow particle flux in the lobe, as presented in Section 3.4. Note that in Figures 1a–1e we have time-shifted the solar wind and IMF data by ~4 min so that the $P_{\rm SW}$ jump coincided with the SYM-H jump to better visualize the different solar wind/IMF conditions before and after the shock. The shock impact caused disturbances in the polar cap ionosphere at ~16:04 UT, as indicated by the jump in the PC(N) index (Figure 1h). Across the shock front, IMF B_z became more negative, IMF

WANG ET AL. 2 of 18

21699402, 2024, 9, Downloaded from https://agupubs.onlinelibrary.wiley.com/doi/10.1029/2024JA032557 by CHIH-PING WANG - University Of California, Los., Wiley Online Library on [15/09/2024]. See the Terms and Conditions (https://onlinelibrary

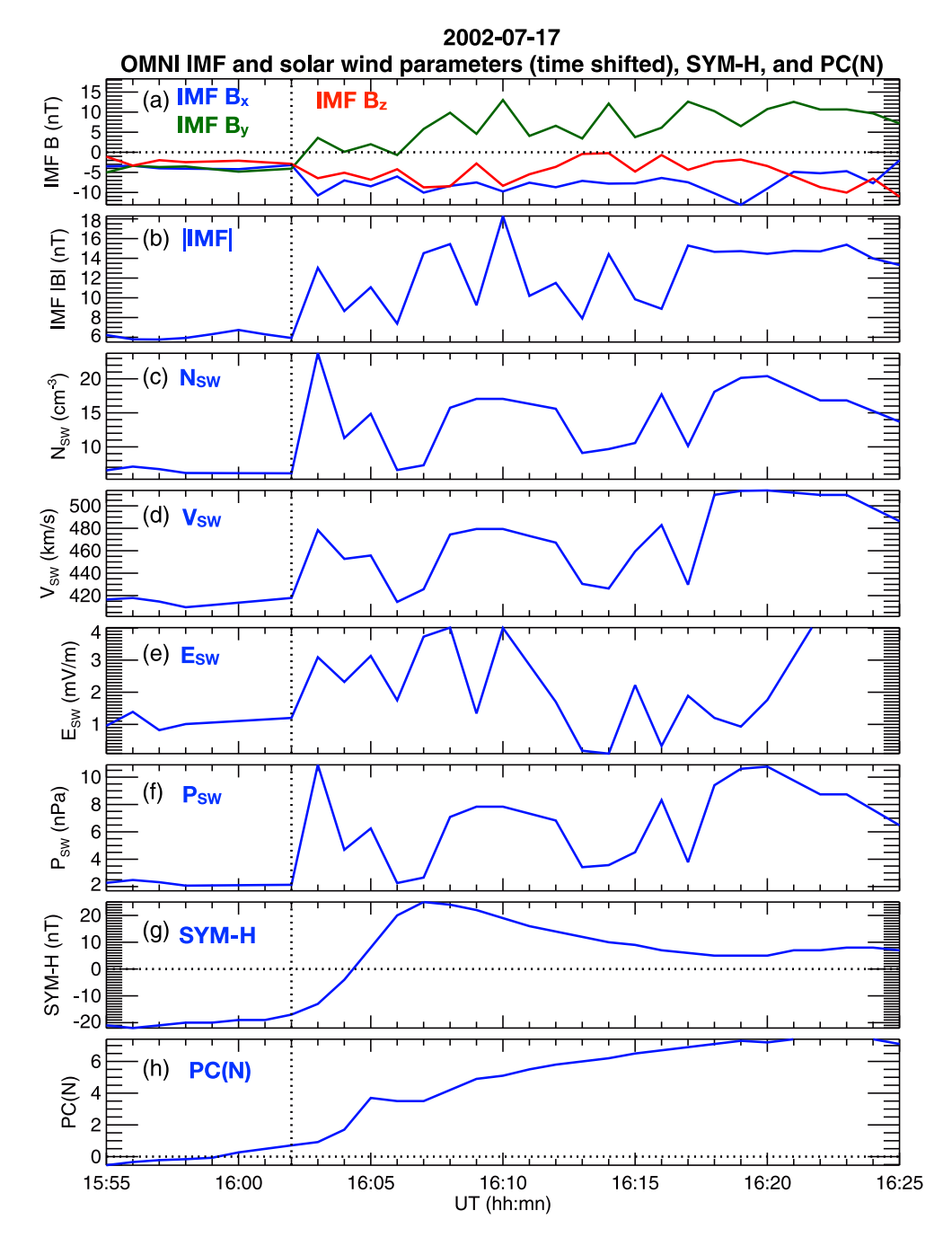


Figure 1. The interplanetary magnetic field (IMF) and solar wind conditions for the interplanetary (IP) shock event on 17 July 2002. (a) IMF components, (b) IMF magnitudes, (c) solar wind number densities, (d) solar wind flow speeds, (e) solar wind electric field, (f) solar wind dynamic pressures, (g) SYM-H index, and (h) PC(N) index from OMNI. The IMF and solar wind parameters have been time shifted so that the start of the IP shock coincides with the jump in SYM-H at 16:02 UT (indicated by the vertical dotted line).

 B_y changed from negative to positive (Figure 1a), and the IMF strength increased by a factor of \sim 2 (Figure 1b). The solar wind density increased by a factor of \sim 3 (Figure 1c) while the solar wind speed only increased slightly (Figure 1d). The resulting solar wind electric field strength increased by a factor of \sim 3–4 and the $P_{\rm SW}$ increased by a factor of \sim 5.

Figure 2 gives an overview of the cluster observations from C1 and C3. The thin lines in Figures 2a and 2b show the X-Z and X-Y projection, respectively, of the trajectories of C1 (blue) and C3 (red) from 15:50 (indicated by the

WANG ET AL. 3 of 18

21699402, 2024, 9, Downloaded from https://agupubs.onlinelibrary.wiley.com/doi/10.1029/2024JA032557 by CHIH-PING WANG - University Of California, Los

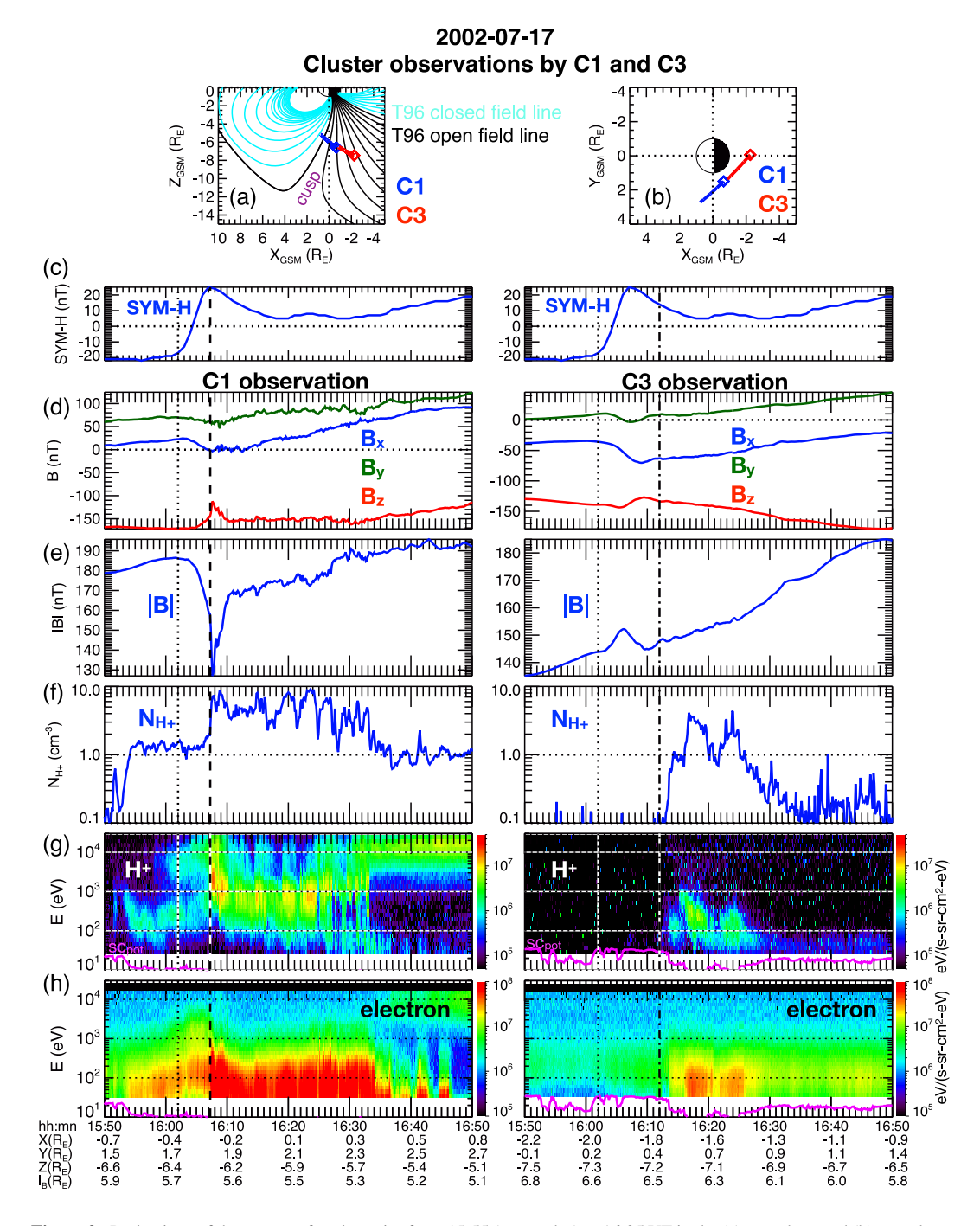


Figure 2. Projections of the spacecraft trajectories from 15:55 (rectangles) to 16:25 UT in the (a) X-Z plane and (b) X-Y plane for C1 (blue) and C3 (red). (c) SYM-H index. Cluster measurements of (d) magnetic field components, (e) magnetic field strength, (f) H^+ density, and energy spectrum of (g) H^+ and (h) electron energy fluxes for C1 (left panels) and C3 (right panels). For the horizontal axis, " I_B " is the field line length from the spacecraft to the ground estimated using the T96 magnetic field. The magenta curves in (g)–(h) indicate spacecraft potential (SC_{pot}).

rectangles) to 16:50 UT. Figure 2a also shows the open (black) and closed (light blue) magnetic field lines from the Tsyganenko 96 (T96) magnetic field model (Tsyganenko, 1995, 1996) with the model input conditions of $P_{\rm SW}=2$ nPa, Dst = -20 nT, IMF $B_y=-5$ nT, and IMF $B_z=-1$ nT corresponding to the observed conditions before the IP shock (Figure 1). The area of the cusp from this magnetic field configuration is indicated. Both C1 and C3 were in the southern hemisphere lobe directly above the polar cap ($X \sim 0$ to -2) near the noon-midnight

WANG ET AL. 4 of 18

meridian ($Y \sim 0$ to 2 R_E). The field-line length from the spacecraft to the ground (see the values of " l_B " in the bottom of Figure 2) was ~ 5.7 and 6.6 R_E for C1 and C3, respectively, at 16:00 UT. They were moving from the nightside toward the dayside, C1 encountered the cusp earlier at $\sim 15:53$ UT while C3 remained in the lobe and did not encounter the cusp until about 60 min later at $\sim 16:57$ UT (see Figure S1f in Supporting Information S1). Figures 2d and 2e show the changes of the Cluster magnetic fields associated with the shock impact at 16:02 UT (indicated by the vertical dotted line) as shown in SYM-H (Figure 2c). Before the impact, B_x was positive at C1 and negative at C3, while at both locations B_y was positive and B_z was negative (Figure 2d). After the impact, B_x at C1 changed from positive to nearly zero, while B_x at C3 became more negative. At both locations, B_z became less negative while the magnitude of $|B_y|$ decreased. The impact caused a |B| decrease at C1 but a |B| increase at C3 (Figure 2e). The observed magnetic field changes are compared with the T96 model fields in Section 3.2.

Figures 2f-2h show the H⁺ ions and electrons observed by Cluster. The magenta curves in the energy spectrum shown in Figures 2g and 2h indicate the spacecraft potential. The left panels show that C1 entered the cusp from the lobe side at ~15:53 UT and then exited the cusp to the dayside plasma sheet at ~16:34 UT. Before the impact, C1 observed both cool (~200 eV) and warm (~5 keV) H⁺ ions and cool electrons (~100 eV), indicating that it was at the edge of the cusp. About 5 min after the impact, at ~16:07 UT, C1 observed a large enhancement in both the H^+ and electron particle fluxes and the H^+ density jumped from ~ 1 to $8~\text{cm}^{-3}$. The peak particle enhancement (indicated by the vertical dashed line) coincided with the significant drop in |B| (Figure 2e), which was a diamagnetic property that indicated that C1 went into the exterior cusp. We investigate in Section 3.3 the pitch angle distributions of the H⁺ particle fluxes within the cusp observed by C1 to show they consisted of both downward- and upward-going ions. On the other hand, C3 was in the lobe before the impact, as indicated by the absence of H⁺ ions and the presence of polar rain electrons. About 10 min after the impact, at ~16:12 UT (indicated by the vertical dotted-dashed line), C3 observed the appearance of both suprathermal H⁺ ions and electrons with H⁺ densities of a few cm⁻³. We investigate in Section 3.4 the plasma moments and the pitch angle distribution of the H⁺ particle fluxes observed by C3 to show that they were outflowing ion beams and ion conics. In Section 3.5 we investigate the C3 measurements for the six outflow drivers and their correlations with the enhanced particle fluxes of the outflowing H⁺ ions.

3.2. Magnetic Field Changes Due To the IP Shock

We compare the magnetic field observed by C1 and C3 with the T96 model magnetic fields to evaluate the field variations due to the changing spacecraft locations and the shock impact. Figures 3a-3d show the X-Z distributions at Y = 1 R_E (we choose a Y location in between C1 and C3, see Figure 2b) of the T96 B_x , B_y , B_z , and B_z , respectively, for a condition before the impact with $P_{SW} = 2$ nPa, Dst = -20 nT, IMF $B_y = -5$ nT, and IMF $B_z = -1$ nT (left panels, fields with subscript of "before"), a condition after the impact with $P_{SW} = 9$ nPa, Dst = +20 nT, IMF $B_y = 2$ nT, and IMF $B_z = -6$ nT (middle panels, fields with a subscript of "after"), and the differences due to the impact (right panels, subtract the fields of "before" from the fields of "after"). The values specified for these before and after the impact conditions are based on the observed values shown in Figure 1. The T96 fields show that, throughout the region from the cusp to the lobe where Cluster spacecraft were moving through during the impact, the magnetopause compression by the P_{SW} jump causes a decrease in B_x and increases in both B_y and B_z . The impact results in a decrease of B_z around the cusp (including the cusp and its immediate vicinity), as observed by C1 (Figure 2e), but an increase in B_z in the lobe, as observed by C3.

Figures 3e–3g compare the Cluster fields with the T96 fields in B_x , B_y , and B_z , respectively. The T96 fields, for both the "before" and "after" fields, are predicted along the Cluster trajectories. The observed fields from 15:55 to 16:02 UT agree quantitatively fairly well with the T96_{before} fields (red dashed lines), indicating the variations are due to spatial variation. For the fields after 16:07 UT, the T96_{after} fields only qualitatively agree with the increasing or decreasing trends of the observed fields. The quantitative field changes due to the impact predicted by the T96 model are relatively better in B_x than in B_y and B_z components. In Section 3.5, we use the differences between the C3 fields and T96_{before} fields (i.e., the differences between the blue line and red dashed lines in Figures 3e–3g) to compute Poynting fluxes associated with the impact. Note that the B_y observed by C3 (the right panel of Figure 3f) showed a bipolar perturbation with a positive perturbation first then a negative perturbation (by comparing with $\langle B_y \rangle$, the 10-min running averages of B_y indicated by the magenta curve) between \sim 16:02 and 16:12 UT. Such bipolar B_y perturbations are also seen in the simulated B_y changes in the lobe (Figures 3e–3g of Paper 2) corresponding to a transient enhancement of upward field-aligned currents (FACs) in response to the

WANG ET AL. 5 of 18

21699402, 2024, 9, Downloaded from https://agupubs.onlinelibrary.wiley.com/doi/10.1099/2024JA032557 by CHIH-PING WANG - University Of California, Los , Wiley Online Library on [1509/2024]. See the Terms and Conditions (https://onlinelibrary.wiley

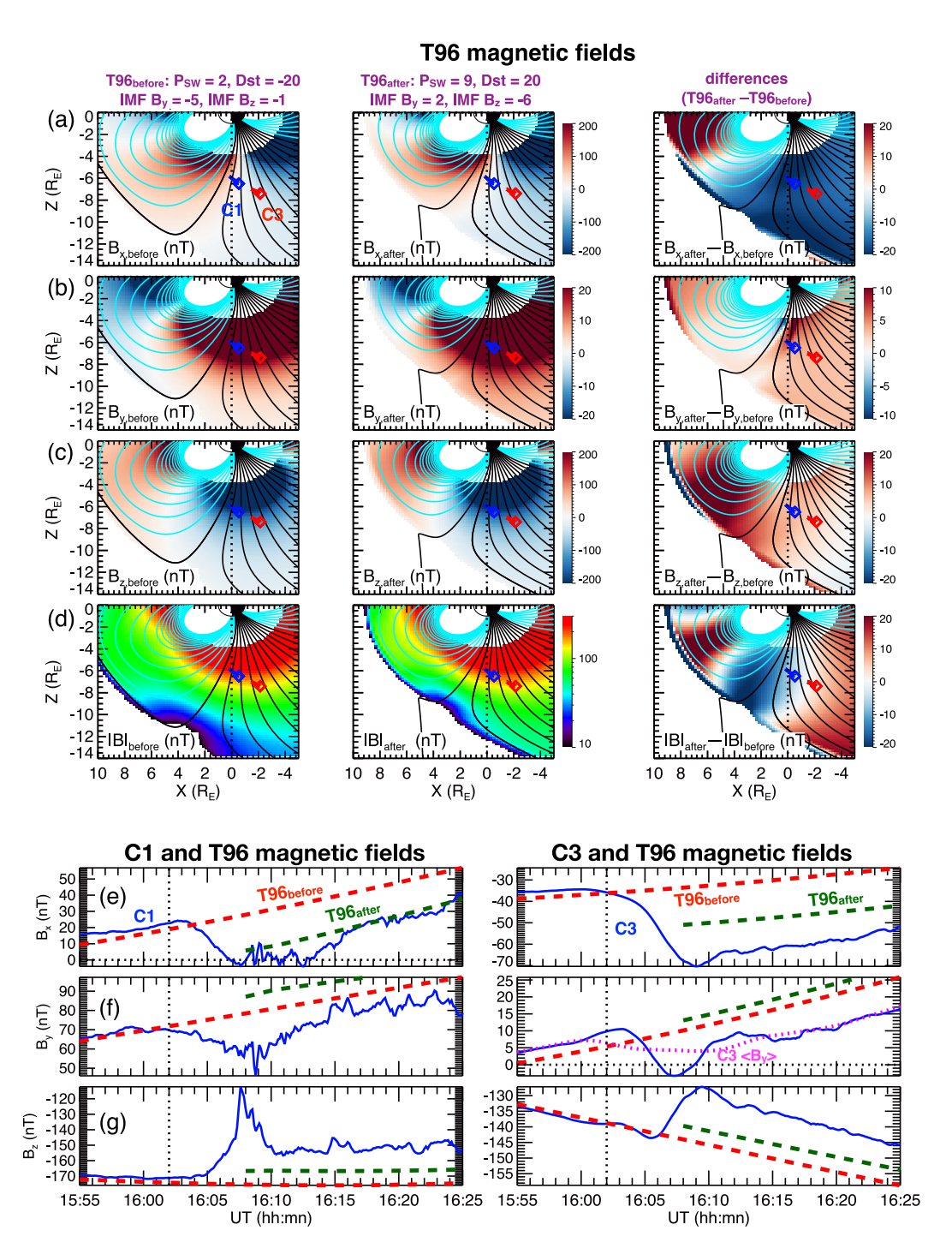


Figure 3. (a)—(d) X-Z profiles (at Y=1 R_E) of the T96 magnetic fields in (a) B_x , (b) B_y , (c) B_z , and (d) B for a pre-shock condition (left panels, T96_{before}: $P_{sw}=2$ nPa, Dst = -20 nT, interplanetary magnetic field (IMF) $B_y=-5$ nT, and IMF $B_z=-1$ nT) and a shock condition (middle panels, T96_{after}: $P_{sw}=9$ nPa, Dst = 20 nT, IMF $B_y=2$ nT, and IMF $B_z=-6$ nT), and the differences (T96_{after} – T96_{before}, right panels). (e)—(f) Cluster measurements (blue lines) of (e) B_x , (f) B_y , and (g) B_z by C1 (left panels) and C3 (right panels) in comparison with T96_{before} (red dashed lines) and T96_{after} (green dashed lines). The 10-min running averages of B_y observed by C3 ($< B_y >$) are indicated by the magenta dotted line in the right panel of (f).

WANG ET AL. 6 of 18

21699402, 2024, 9, Downloaded from https://agupubs.onlinelibrary.wiley.com/doi/10.1029/2024JA032557 by CHIH-PING WANG - University Of California, Los , Wiley Online Library on [15/09/2024], See the Terms

2002-07-17, C1 observations of H+ ions

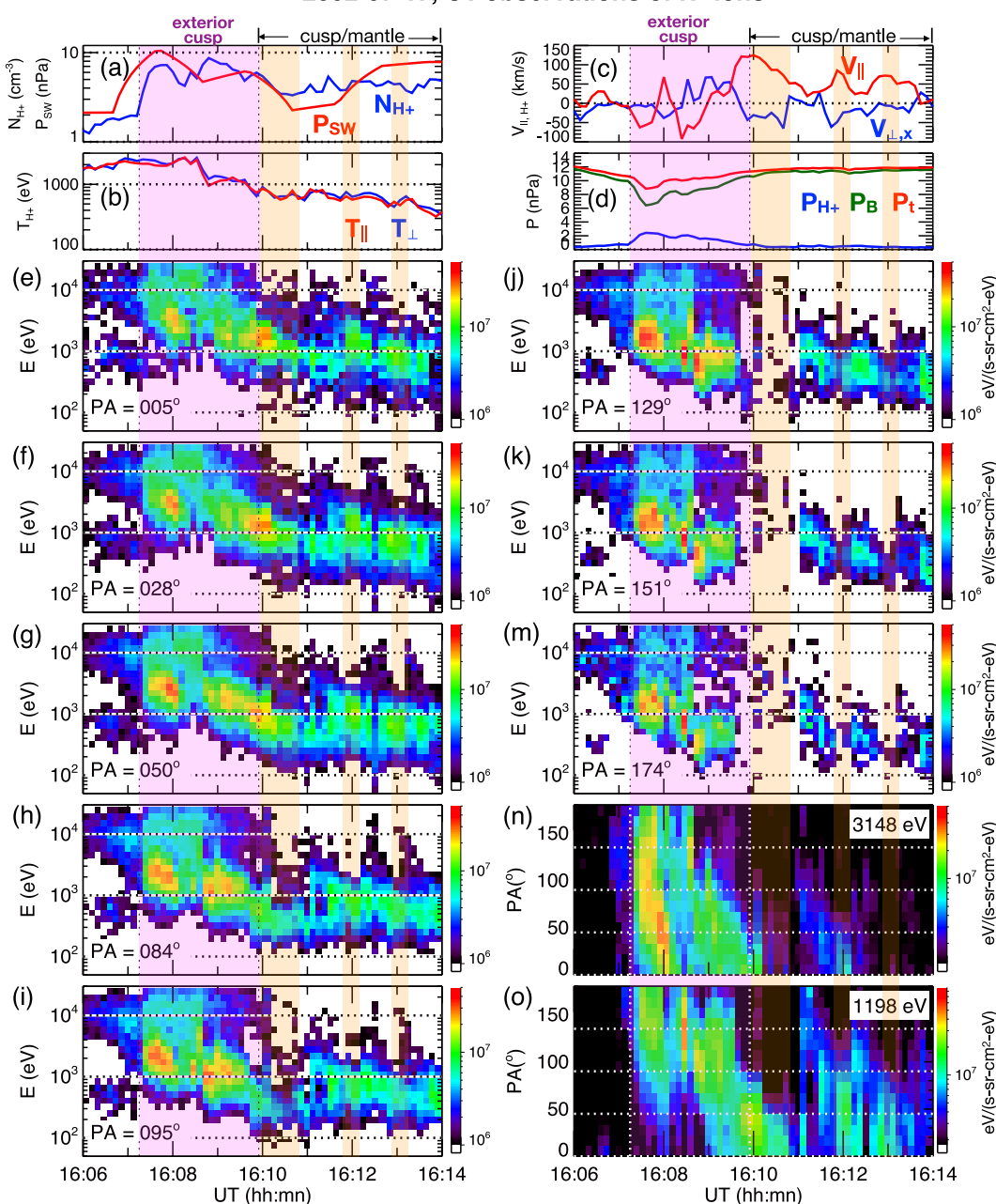


Figure 4. C1 measurements of H^+ ions from 16:06 to 16:11 UT. (a)–(d) The H^+ moments: (a) densities, (b) parallel (red) and perpendicular (blue) temperatures, (c) pressures (plasma pressure in blue, magnetic pressure in green, and total pressure in red), and (d) parallel (red) and perpendicular (blue) bulk flow speeds. (e–m) Energy spectrum of H^+ particle energy fluxes at 8 pitch angles (PA = 5° , 28° , 50° , 84° , 95° , 129° , 151° , 174°). The particle energy fluxes as a function of PA for (n) 3,148 eV and (o) 1,198 eV H^+ ions. The purple-shaded interval indicates the exterior cusp. The orange-shaded intervals indicate the times of observing ion conics.

WANG ET AL. 7 of 18

shock impact. As discussed in Section 4, associated with enhancing upward FACs, a parallel upward electric field might develop and accelerate the polar wind ions to ion beams.

3.3. Changes in the Cusp Due To the IP Shock Observed by C1

In this section, we show that C1 observed large changes in the plasma moments and magnetic fields due to encountering the exterior cusp after the shock impact. As shown in Figure 2, C1 was already in the vicinity of the cusp before the shock impact. Figure 4 shows that a few minutes after the impact, at ~16:07:15 UT, C1 observed a sharp jump in H⁺ density from ~2 to 8 cm⁻³ (Figure 4a) and enhancements of H⁺ particle fluxes at all pitch angles (Figures 4e-4m). From 16:07:15 to 16:09:55 UT (purple-shaded interval), the H⁺ density remained high and the H^+ temperatures were > 1 keV (Figure 4b), and the resulting enhanced plasma pressure (blue line in Figure 4d) and depressed magnetic pressure (green line in Figure 4d) indicated the diamagnetic signature of the exterior cusp. The H⁺ bulk field-aligned flow $(V_{\parallel}, \text{ red line in Figure 4c})$ was mainly downward within the exterior cusp and mainly upward after 16:09:30 UT. Lavraud et al. (2004, 2005) used Cluster observations to establish statistically the spatial distributions of the cusp and showed altitudinal variations of the plasma moments from the region of the exterior cusp (within approximately 2 R_E inside the magnetopause, for example, see Figure 3 of Lavraud et al. (2004)) to the cusp region below. Compared with their statistical altitudinal variations, the different cusp plasma moments inside and outside the exterior cusp observed by C1 in this event were consistent with the differences seen between the exterior cusp and the cusp below. Similarly, comparing with the statistical distribution of V_{\parallel} shown in Figure 4 of Lavraud et al. (2005) suggests that C1 was likely in the cusp/mantle transition region during the upward-flow-dominated interval after ~16:09 UT. Since C1 was moving very slowly and toward lower altitudes (Figure 2), this consistency indicates that the above encounter of the exterior cusp by C1 should be due to the region of the exterior cusp being pushed downward to the C1 altitudes as the magnetopause was compressed by the P_{SW} jump (red line in Figure 4a).

Figures 4e-4m show the energy spectrum of H⁺ energy fluxes at 8 different pitch angles, and Figures 4n and 4o show the energy fluxes as a function of pitch angle for 3,148 and 1,198 eV H⁺ ions, respectively (see Figure S2 of Supporting Information S1 for other energy channels). Since Cluster spacecraft were in the southern hemisphere at the time, thus the parallel direction (PA $< 90^{\circ}$) was upward from the ionosphere while the anti-parallel direction $(PA > 90^{\circ})$ was downward. Within the exterior cusp (purple-shaded interval), the particle fluxes were enhanced at a few keV and in all pitch angles with relatively higher fluxes around the perpendicular direction than along the two field-aligned directions (see Figure 4n). This is quantitatively similar to the simulated pitch-angle distribution within the exterior cusp for the H⁺ ions from the solar wind (see Figure 6b of Paper 2 for $t \sim 33-37$ min). During the interval after ~16:09:50 UT when C1 was likely in the cusp/mantle boundary, for most of the time it observed similar particle fluxes in all pitch angles with relatively larger fluxes in the upward direction than the downward direction. This pitch-angle distribution is similar to the simulated pitch-angle distribution in the cusp/mantle transition region for the H $^+$ ions from the solar wind (see Figure 6b of Paper 2 for t > 37 min). During the upwardflow-dominated interval C1 also observed ion conics for a few very brief intervals (orange shaded) (see Figure 40). This conic distribution is characteristically similar to the simulated pitch-angle distribution within the cusp and mantle regions for the outflow H⁺ ions from the ionosphere (see Figure 6d of Paper 2). Thus, the observed mixture of the two characteristically different pitch-angle distributions suggests the co-existence of H⁺ ions from the solar wind and the ionosphere in the cusp/mantle region.

3.4. Outflowing H⁺ Ions in the Lobe After the IP Shock Impact Observed by C3

We show in Figure 5 that C3 in the lobe observed outflowing H⁺ ions that appeared ~10 min after the shock impact. Note that around the same time similar outflowing H⁺ ions were also observed by C4, which was ~0.6 R_E from C3. The outflowing H⁺ ions had density up to ~4 cm⁻³ (Figure 5a), temperature of ~100–500 eV (Figure 5b), field-aligned upward flow speed of ~60 km/s (red line of Figure 5c), and perpendicular flow speed of ~5 km/s in the X-direction (blue line in Figure 5c). The associated plasma pressure (blue line in Figure 5d) was two orders of magnitudes smaller than the magnetic pressure (red line in Figure 5d). Figures 5e–5n show that the H⁺ particle fluxes were mainly in the parallel direction (i.e., outward in the southern lobe). The flux increase consisted of three succeeding enhancements (indicated by "1," "2," and "3" on the top of Figure 5a and the vertical dotted lines) with the energy range (the range is indicated approximately by the two magenta dotted lines in the PA = 5° energy spectrum of Figure 5e) becoming higher and the pitch-angle distribution changing from ion beams to ion conics. This change in pitch-angle distribution can be seen in Figures 5o and 5p for the energy fluxes

WANG ET AL. 8 of 18

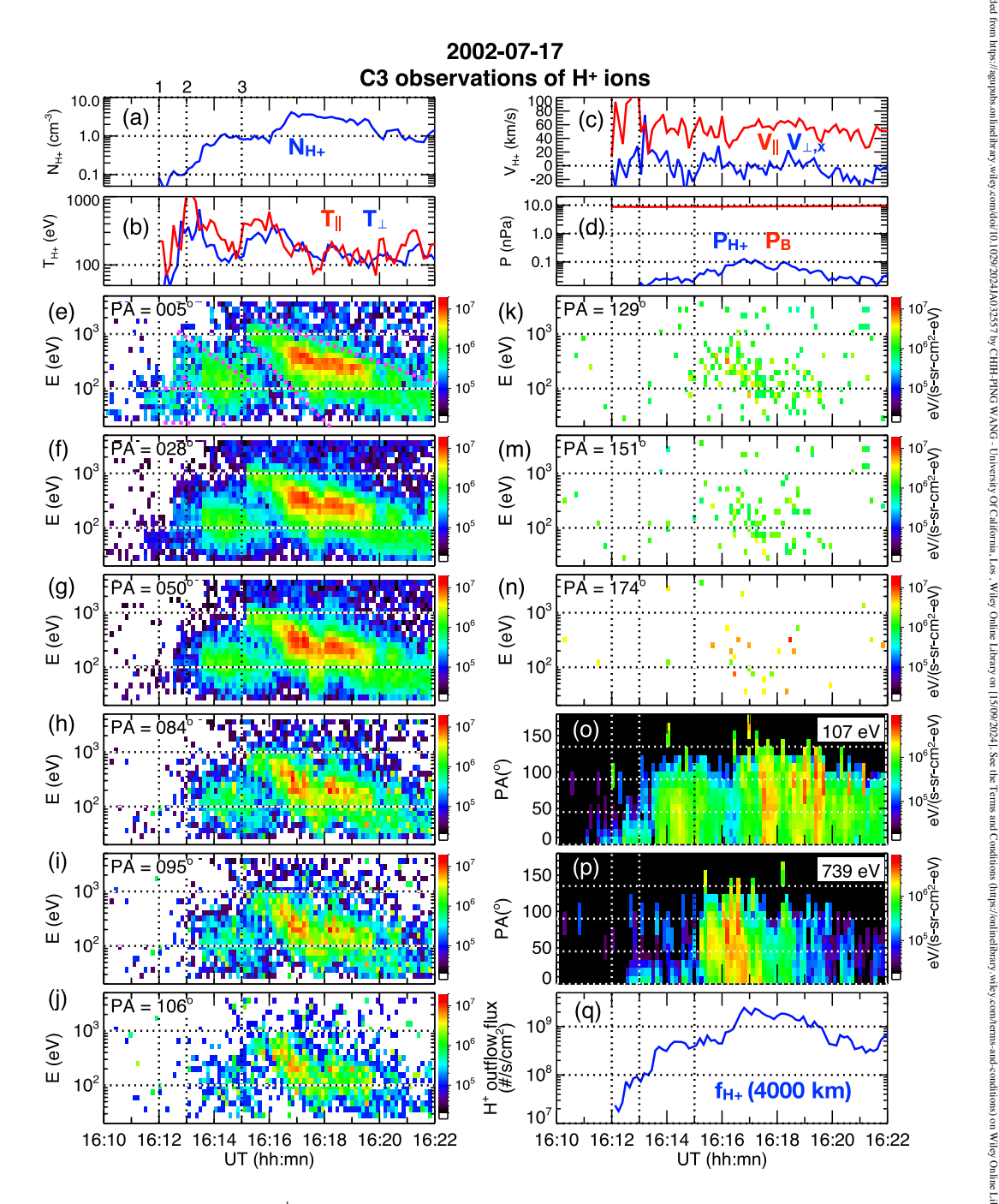


Figure 5. C3 measurements of H^+ ions from 16:10 to 16:22 UT. (a) Densities, (b) parallel (red) and perpendicular (blue) temperatures, (c) pressures (plasma pressure in blue and magnetic pressure in red), and (d) parallel (red) and perpendicular (blue) bulk flow speeds. (e-n) The H^+ particle energy fluxes at 9 pitch angles (PA = 5° , 28° , 50° , 84° , 95° , 106° , 129° , 151° , 174°). The particle energy fluxes as a function of PA for (o) 107 eV and (p) 739 eV H^+ ions. (q) The H^+ outflow flux mapped from the C3 altitude to 4,000 km altitude.

as a function of pitch angle for 107 and 739 eV, respectively (the pitch-angle distributions for other energy channels are shown in Figure S3 of Supporting Information S1). The first enhancement was from \sim 16:12:00 to 16:13:00 UT, the second one was from \sim 16:13:00 to 16:15:00 UT, and the third one was from \sim 16:15:00 to \sim 16:22:00 UT. The first enhancement was seen at energies $<\sim$ 100 eV and was highly field-aligned with substantial fluxes only seen within small pitch angles (PA < 30°). The second enhancement started with the appearance of highly field-aligned and relatively higher energy H⁺ ions (up to \sim 1,000 eV) followed by the

WANG ET AL. 9 of 18

appearance of lower energy H⁺ ions (up to $\sim 200 \, \text{eV}$) with pitch angles extending to a larger range (PA < $\sim 106^\circ$). The pitch angle distributions of the first and second enhancements showed the signature of ion beams (the maximum flux is at PA $\sim 0^\circ$). The third enhancement was similar to the second enhancement in terms of higher energy particles appearing first, but the overall energy was higher, and the pitch-angle distribution showed the signature of ion conics (the maximum fluxes were at $\sim 50^\circ$ from $\sim 16:16:00$ to 16:20:00 UT). Note that from $\sim 16:15:00$ to 16:16:00 UT, there was a co-existence of $\sim 100 \, \text{eV}$ particles from the second enhancement and $\sim 1,000 \, \text{eV}$ particles from the third enhancement. From the first to the third enhancements, the flux values increased by more than an order of magnitude. As discussed in Section 4, the above changes in the energies and pitch-angle distributions may be a result of acceleration by multiple mechanisms.

The outflowing H^+ ions observed by C3 was not likely due to the encounter with the cusp. Since C1 and C3 were in the string-of-pearls formation, if the cusp region did not change, then C3 would cross the same cusp region crossed by C1 earlier. But the time lag between C1 and C3 was about 50 min, and C3 did not encounter the cusp until \sim 16:57 UT. Since the magnetopause was compressed by the IP shock, the cusp region might move even when C3 only moved \sim 0.3 R_E from 16:00 to 16:10 UT (see Figure 2). However, the pitch-angle distribution of the H⁺ ions observed by C3 was characteristically different from that of the cusp H⁺ ions observed by C1, indicating that the appearance of the outflowing H⁺ ions was not likely a result of the cusp being pushed tailward to the C3 location by the magnetosphere compression due to the shock impact. Thus, it is more likely that the H⁺ ion beams and conics came upward from the polar cap, not due to an encounter with the cusp.

Figure 5q shows the calculated field-aligned fluxes for the outflowing H⁺ ions (e.g., Zhao et al., 2020), $f_{\rm H+} = \int f 2\pi \cdot J(E, \theta) \cos(\theta) \sin(\theta) {\rm d}\theta {\rm d}E$, where J is differential energy flux, E is particle energy from 30 eV to 30 keV, and θ is pitch angle from 0° to 90° (for outward direction only). For comparison with the results from previous studies (e.g., Zhao et al., 2020), the computed $f_{\rm H+}$ values at the C3 location are then mapped to 4,000 km altitude using $f_{\rm H+}/B$ = constant, where the B strength at C3 was from the observation and at the 4,000 km altitude is from the T96_{before} fields. The $f_{\rm H+}$ values increased from ~2·10⁷ #/s/cm² to the peak value of 3·10⁹ #/s/cm² in about 5 min then decreased. Note that this 5-min time scale was similar to that seen in the initial increase of SYM-H (Figure 1f) we described in Section 3.1. In comparison, the statistical $f_{\rm H+}$ values around the cusp are from 10⁵ to 10^9 #/s/cm² as observed by the FAST satellite at ~4,000 km altitudes (Zhao et al., 2020).

3.5. Outflow Drivers and Correlations With H⁺ Outflow Flux Observed by C3

In this section, we investigate the changes in the six outflow drivers described in Introduction due to the shock impact observed by C3 and show that the initial increase of DC Poynting fluxes was well correlated with the initial increase of $f_{\rm H+}$ observed by C3 ~8 min later. We examine in Figures 6 and 7 the six drivers: (a) Downward field-aligned DC Poynting flux $(S_{\rm DC,\parallel})$; (b) downward field-aligned AC Poynting flux $(S_{\rm AC,\parallel})$; (c) electric field amplitude of extremely low frequency (ELF) waves $(A_{\rm ELF})$; (d) Precipitating electron density $(n_{\rm ep})$; (e) precipitating electron number flux $(f_{\rm en})$; (f) Precipitating electron energy flux $(f_{\rm ee})$.

Note that since C3 started to observe outflowing H⁺ ions after ~16:12 UT, we only investigate the changes in the six drivers before 16:12 UT. For computing the DC and AC Poynting fluxes, we use the methodology of the previous studies (e.g., Strangeway et al., 2000; Zhao et al., 2020), which assumes that the magnetic field $\mathbf{B} = \mathbf{B}_0 + \delta \mathbf{B}$, where \mathbf{B}_0 is a background field and $\delta \mathbf{B}$ is a perturbation field. In this study, we use \mathbf{B}_{T96} before as the **B**₀. Figure 6 shows the calculated Poynting fluxes $S = E \times \delta B/\mu_0$ from the electric fields and magnetic fields observed by C3, where $\delta \mathbf{B} = \mathbf{B}_{\text{C3}} - \mathbf{B}_{\text{T96, before}}$ (see the right panels of Figures 3e–3g, blue lines are \mathbf{B}_{C3} and red dashed lines are $\mathbf{B}_{T96, before}$). The observed electric drift and electric fields are shown in Figures 6a and 6b, respectively. The magnetic field perturbations are further divided into two different frequency ranges, $\delta \mathbf{B} = \delta \mathbf{B}_{\mathrm{DC}} + \delta \mathbf{B}_{\mathrm{AC}}$, where $\delta \mathbf{B}_{\mathrm{DC}}$ is for <0.1 Hz (Figure 6c, $\delta \mathbf{B}_{\mathrm{DC}}$ is 10 s running averages of $\delta \mathbf{B}$) and $\delta \mathbf{B}_{\mathrm{AC}}$, is for >0.1 Hz (Figure 6d). The Poynting flux is thus divided into the DC Poynting flux ($\mathbf{S}_{DC} = \mathbf{E} \times \delta \mathbf{B}_{DC}/\mu_0$) and AC Poynting flux ($S_{AC} = E \times \delta B_{AC}/\mu_0$). The parallel DC ($S_{DC,\parallel}$) and AC Poynting fluxes ($S_{AC,\parallel}$) mapped to the 4,000 km altitude using S/B constant are shown in Figures 6e and 6f, respectively. The intensity of the downward $S_{\rm DC,\parallel}$ ($S_{\rm DC,\parallel,down}$, i.e., negative $S_{\rm DC,\parallel}$ values indicated by blue-shaded intervals) increased from ~16:04 UT to \sim 16:09 UT and then quickly decreased afterward. The $S_{\mathrm{DC},\parallel,\mathrm{down}}$ increase was due to increases in the intensity of both E and $\delta \mathbf{B}_{DC}$ while the $S_{DC,\parallel,down}$ decrease corresponded to a decrease in E. This \sim 5 min time scale in the $S_{\text{DC},\parallel,\text{down}}$ increase was similar to those seen in the initial increase of SYM-H (Figure 1f) and the initial increase of

WANG ET AL. 10 of 18

https://agupubs.onlinelibrary.wiley.com/doi/10.1029/2024JA032557 by CHIH-PING WANG - University Of California, Los , Wiley Online Library on [15/09/2024]. See the Terms

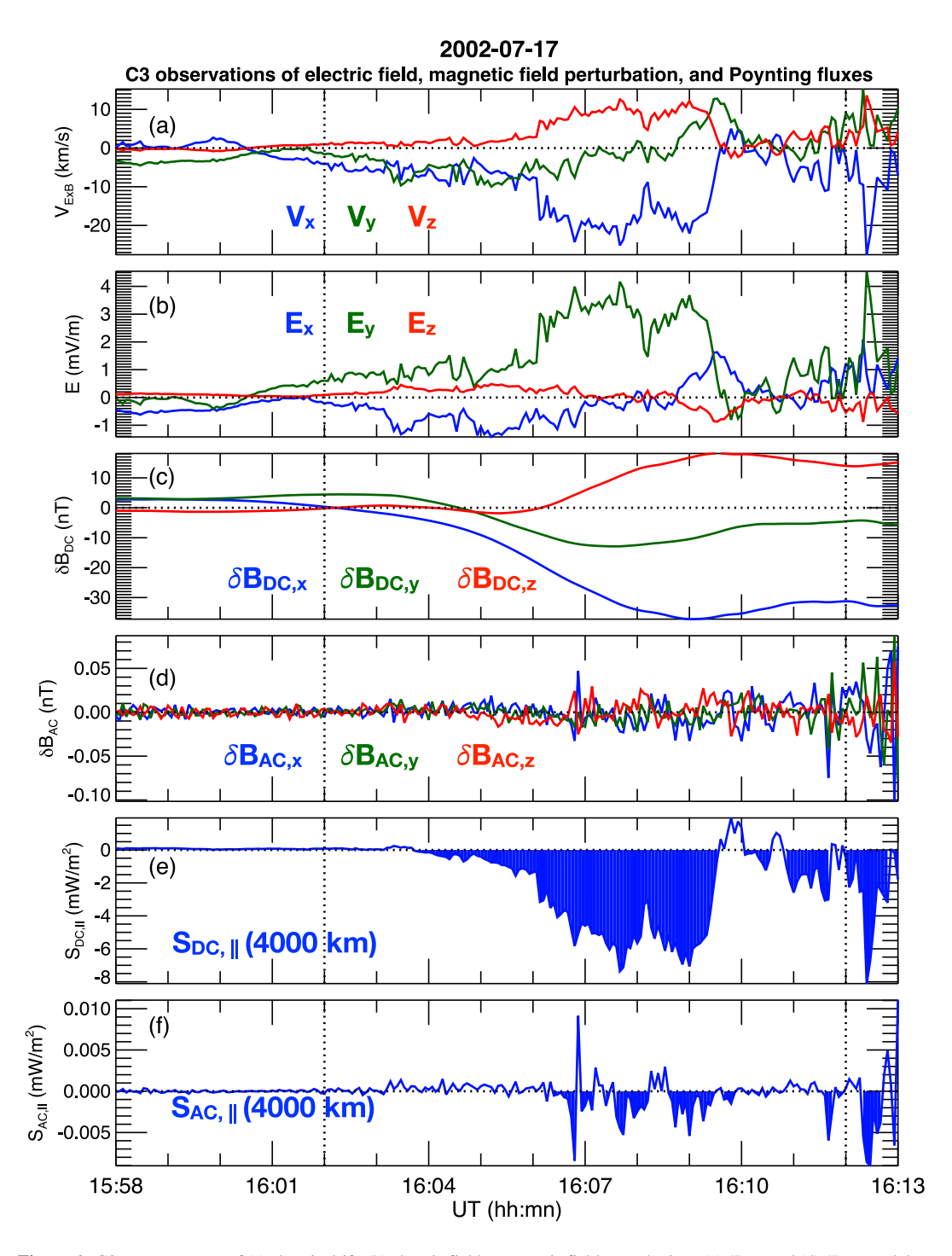


Figure 6. C3 measurements of (a) electric drift, (b) electric fields, magnetic field perturbations (c) δB_{DC} and (d) δB_{AC} , and the field-aligned (e) DC and (f) AC Poynting fluxes mapped from the C3 altitudes to 4,000 km altitude.

 $f_{\rm H+}$ (Figure 5q). Compared with the increase in $S_{\rm DC, \parallel, down}$ being continuous, Figure 6f shows that $S_{\rm AC, \parallel, down}$ was only enhanced sporadically from ~16:06 to 16:10 UT with large fluctuations in the intensity.

Compared to the DC Poynting fluxes, the shock impact did not cause substantial enhancements in $A_{\rm ELF}$, $n_{\rm ep}$, $f_{\rm en}$, and $f_{\rm ee}$ before the appearance of outflowing H⁺ ions. Figure 7a shows the power spectrum density of electric field power within the frequency range of 8–4,000 Hz and Figure 7b shows the corresponding values of $A_{\rm ELF}$. Before the H⁺ outflow, there were a few very brief (less than a minute) increases of $A_{\rm ELF}$ at ~16:02, 16:06, and 16:11 UT.

WANG ET AL. 11 of 18

21 699402, 2024, 9, Downloaded from https://agupubs.onlinelibrary.wiley.com/doi/10.1029/2024JA032557 by CHIH-PING WANG - University Of California, Los, Wiley Online Library on [15/09/2024]. See the Terms and Conditions

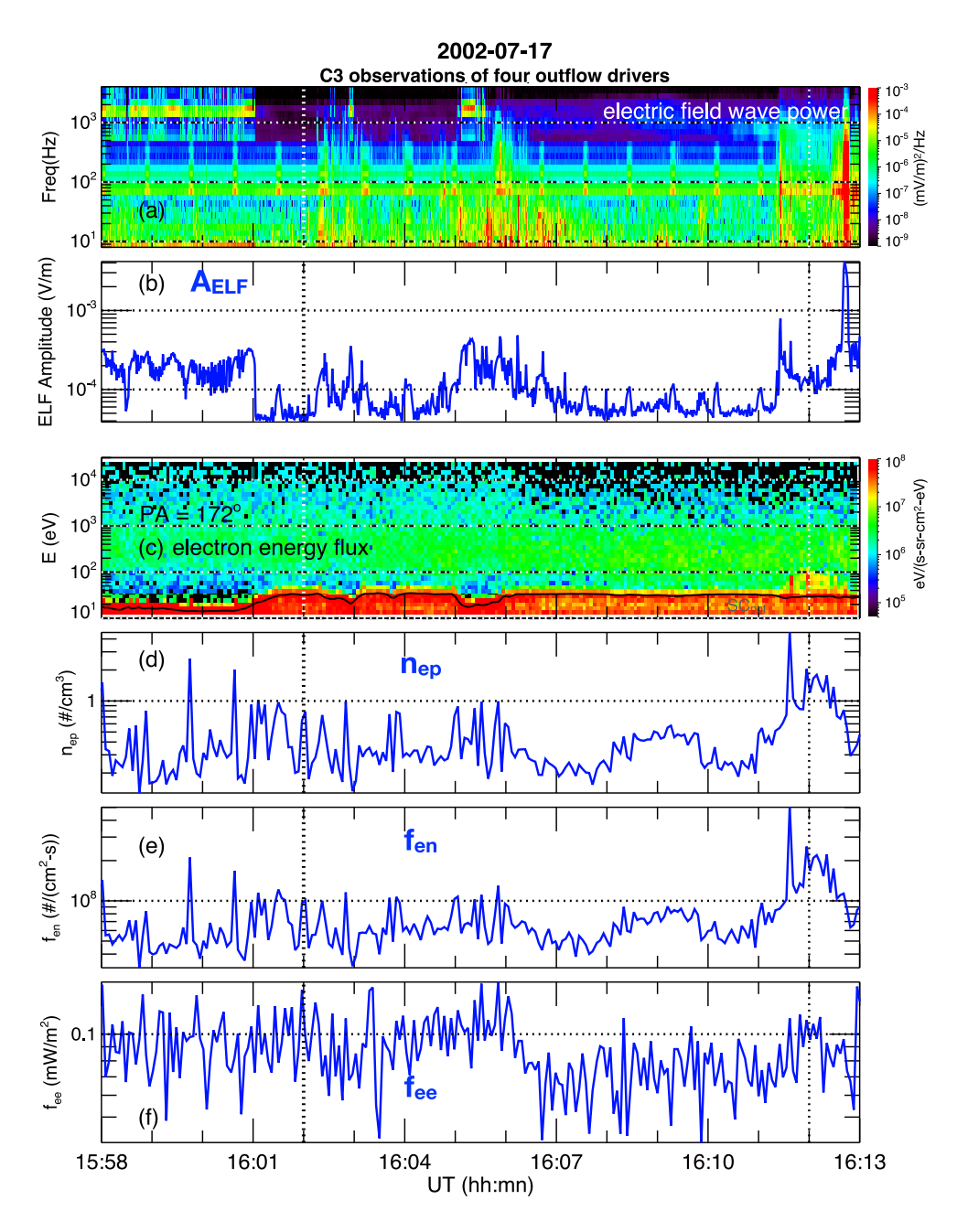


Figure 7. C3 measurements of (a) electric field power spectrum and (b) amplitude of extremely low frequency waves computed from (a). (c) Electron energy fluxes at pitch angle = 172° . The gray curve indicates the spacecraft potential. The three drivers associated with electron precipitating (d) density $(n_{\rm ep})$, (e) number flux $(f_{\rm en})$, and (f) energy flux $(f_{\rm ee})$ computed from (c).

Figure 7c shows the electron energy fluxes at PA = 172° (the black curve indicates the spacecraft potential). We assume these fluxes represent those within the loss cone for the electron precipitation and the corresponding $n_{\rm ep}$, $f_{\rm en}$, and $f_{\rm ee}$ (integrated over the energy range from the spacecraft potential to 20 keV) are shown in Figures 7d–7f, respectively. Comparing the values 10 min before and 10 min after the impact, there were no clear changes in the electron fluxes and the values of the associated $n_{\rm ep}$, $f_{\rm en}$, and $f_{\rm ee}$.

We plot in Figure 8 the H^+ outflow fluxes (Figure 8a, the same as Figure 5q) with the six outflow drivers (Figure 8b–8g). As described above, both the initial increase in the H^+ outflow fluxes and the initial increase in the DC Poynting fluxes had a similar time scale of \sim 5 min. Since there was a time delay between their starting times, to

WANG ET AL. 12 of 18

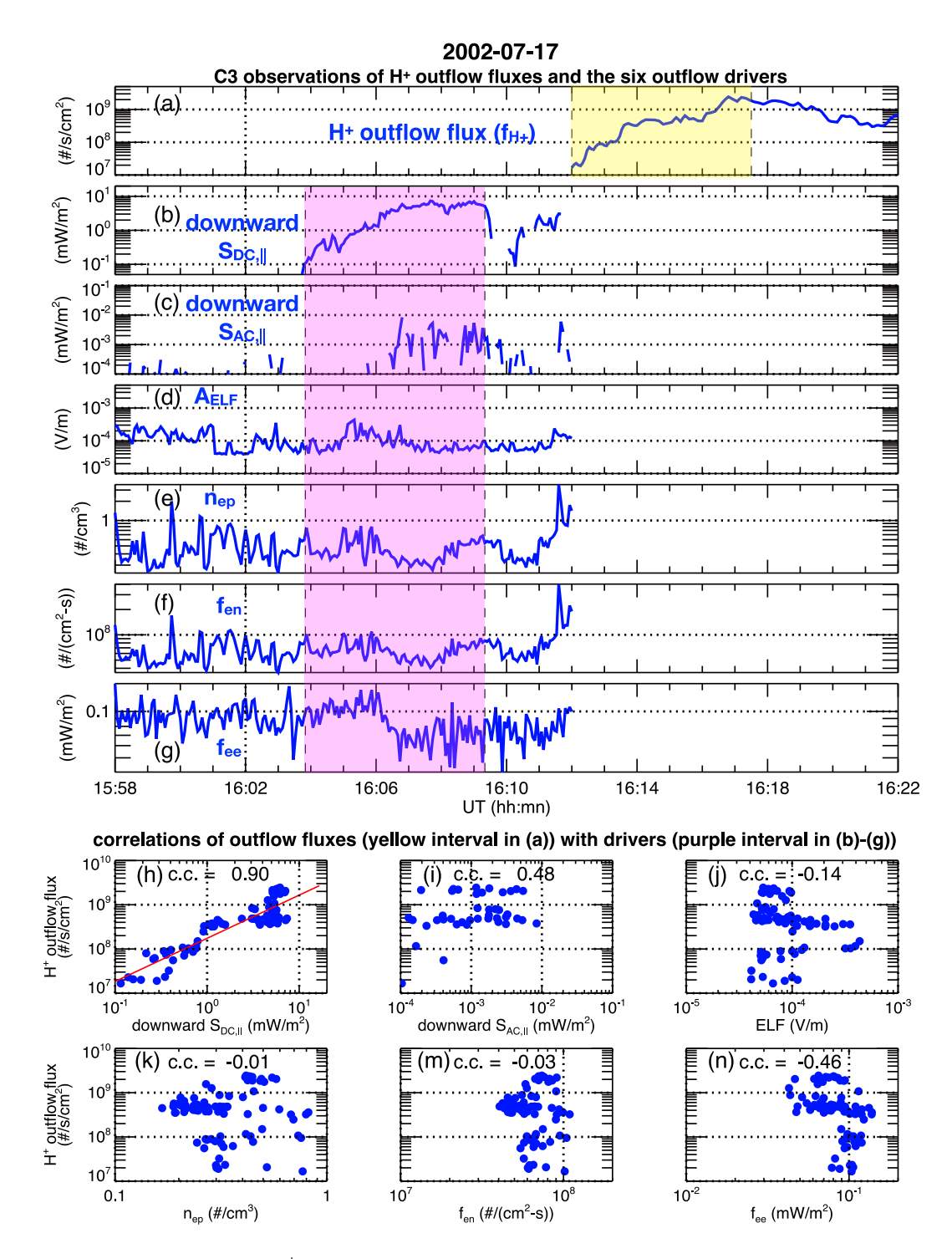


Figure 8. C3 observations of (a) H⁺ outflow fluxes, and the six drivers: (b) downward $S_{\rm DC,||}$, (c) downward $S_{\rm AC,||}$, (d) $A_{\rm ELF}$, (e) $n_{\rm ep}$, (f) $f_{\rm en}$, and (g) $f_{\rm ee}$. The correlations of the outflow fluxes from 16:13:30 to 16:219:00 UT (yellow-shaded interval in (a)) with the six drivers from 16:04:00 to 16:09:30 UT (purple-shaded interval in (b)–(g)) for (h) downward $S_{\rm DC,||}$, (i) downward $S_{\rm AC,||}$, (j) $A_{\rm ELF}$, (k) $n_{\rm ep}$, (m) $f_{\rm en}$, and (n) $f_{\rm ee}$.

investigate their correlations, we take the $f_{\rm H+}$ data within a window of 330 s starting from its first appearance at 16:12:00 UT (yellow-shaded region in Figure 8a) and correlate them with the $S_{\rm DC,II,down}$ data within the same 330-s window from its first appearance at 16:03:50 UT (purple-shaded region in Figure 8b). As shown in Figure 8h, they were highly correlated with the correlation coefficient of 0.9. The linear fit of this correlation (red line in Figure 8h)

WANG ET AL. 13 of 18

gives $f_{\rm H+} = 10^{8.6} S_{\rm DC, \parallel, down}^{0.85}$ (#/s/cm²) at 4,000 km altitude. Compared with the statistical results of the H⁺ outflow fluxes in the cusp by Zhao et al. (2020), for the same intensity of the DC Poynting fluxes, the H⁺ outflow fluxes observed in the lobe during this IP shock event were about an order of magnitude larger. For the other five drivers, since they did not have a clear increase during the ~5 min purple-shaded interval after the shock impact (Figures 8c–8g), they were not correlated with the increasing outflow fluxes, as shown in Figures 8i–8n.

The observed enhancements in the electric fields, magnetic field DC perturbations, and downward field-aligned DC Poynting fluxes caused by the shock impact shown in Figure 6 are also seen in the simulation results (see Figures 7a–7f of Paper 2). The simulation also shows that the enhanced downward DC Poynting fluxes increase the numbers of H⁺ ions coming out of the polar-cap ionosphere, and that these ions reach the high-latitude lobe a few minutes later with a pitch-angle distribution of ion conics (see Figures 7f–7g of Paper 2). Thus, the simulation supports that the outflowing H⁺ ions observed by C3 in the lobe were plausibly outflows from the polar cap.

4. Discussion

The enhanced downward DC Poynting fluxes were observed by C3 in the lobe about 2 min after the IP shock impact and then, after \sim 8 min, outflowing H⁺ ions appeared in the southern lobe. The outflowing ions started with ion beams at $<\sim$ 100 eV and were followed by ion conics of several hundreds of eV, suggesting that multiple acceleration mechanisms were involved. A good correlation was found between the increasing downward DC Poynting fluxes and the increasing outflow fluxes. Here, we discuss possible explanations and conclude that these outflowing H⁺ ion beams and conics were likely a result of the acceleration of pre-existing polar wind ions driven by the enhanced Poynting fluxes.

Based on previous studies (e.g., Strangeway et al., 2005), downward Poynting fluxes is one of the energy sources to drive ionospheric outflows, and there are two ways the downward Poynting fluxes can contribute to ionospheric H⁺ outflows: (a) Poynting fluxes go down to the ionosphere F region (~150–500 km altitude) and cause Joule dissipation, which heats ions sufficiently to cause ion upwelling and thus provide more source ions for generating outflow H⁺ ions as the polar wind above ~1,000 km altitude. The observed average temperature of the H^+ polar wind ions is $< \sim 2$ eV (Su, Horwitz, Moore, et al., 1998; Su, Horwitz, Wilson, et al., 1998; Yau et al., 2007). (b) Poynting fluxes reaching down to altitudes of ~1,000 km to 15,000 km can cause acceleration of the polar wind to generate suprathermal outflow ions, including the ion beams associated with parallel acceleration and ion conics associated with perpendicular acceleration. The parallel acceleration can be due to the upward quasi-static parallel electric field (e.g., Lu et al., 1992) associated with upward FACs. The altitude of such a parallel electric field is below ~15,000 km (e.g., Ergun et al., 2004; Reiff et al., 1993). The perpendicular acceleration can be due to the interaction with different wave modes, such as ion cyclotron waves (e.g., Chang et al., 1986; Crew et al., 1990), broadband waves (e.g., André et al., 1990), lower hybrid waves (e.g., Chang & Coppi, 1981), and dispersive Alfvén waves (e.g., Chaston et al., 2004). This wave acceleration typically occurs below ~10,000 km (e.g., Moore & Horwitz, 2007). It is thus expected that, through these acceleration processes, the larger energy source going down would result in more suprathermal outflow ions coming out. This expected good correlation has been shown statistically in the previous studies using the observations from a satellite at ~4,000 km altitude (e.g., Strangeway et al., 2005; Zhao et al., 2020). As the suprathermal outflow ions moving upward from the acceleration altitudes, this good correlation should continuously be seen at higher altitudes but with a time delay, which plausibly explains the C3 observations at $\sim 6 R_E$ altitude that the initial increase in the outflow fluxes was well correlated with the initial enhancements of the downward DC Poynting fluxes several minutes earlier.

In this event, C3 observed the suprathermal outflowing H^+ ion beams and ion conics, indicating that the observed enhanced Poynting fluxes led to the acceleration of the polar wind. Based on the two ways Poynting fluxes affect outflows described above, we consider two scenarios illustrated in Figure 9 and make simple estimations of the times needed for H^+ suprathermal outflows to reach the C3 altitude (\sim 6.5 $R_{\rm E}$) after enhanced Poynting fluxes reached down to lower altitudes. We assume that the time for Poynting fluxes propagating downward from C3 to the ionosphere is negligibly short.

1. The first scenario consists of two steps (Figure 9a). First, the enhanced downward Poynting fluxes reached the F region and enhanced upwelling ions to generate more polar wind ions, and during the second step these polar wind ions were then accelerated by processes driven by enhanced Poynting fluxes reaching down to altitudes above 1,000 km. Considering that the upwelling speed increases linearly from 0 at 400 km altitude to ∼1 km/s

WANG ET AL. 14 of 18

polar cap

21699402, 2024, 9, Downloaded from https://agupubs.onlinelibrary.wiley.com/doi/10.1029/2024JA032557 by CHIH-PING WANG - University Of California, Los

Two proposed scenarios for the ion beam and ion conics observed by C3 (a) Scenario 1 (b) Scenario 2 altitude altitude 6 Re Poynting flux Poynting flux on beam 15,000 km 15,000 km polar wind 1000 km Poynting flux upwelling $(V_{\parallel} < 1 \text{ km/s})$ polar wind 400 km 1000 km F region Joule heating

Figure 9. The processes proposed for producing the ion beam and ion conics observed by Cluster C3 are illustrated in (a) for scenario 1 and (b) for scenario 2.

polar cap

at 1,000 km altitude (e.g., Endo et al., 2000), it would take \sim 25 min for upwelling ions to move from 400 to 1,000 km altitude to generate the source for the polar wind. Thus, this first step alone takes much more time than the 8-min delay. Even without including this first step, we can consider the second step alone as the second scenario.

2. In the second scenario (Figure 9b), there were pre-existing polar wind ions and they were accelerated due to enhanced Poynting fluxes reaching altitudes above 1,000 km. Note that C3 would not observe such pre-existing H⁺ polar wind ions because their thermal energy of ~1 eV was substantially lower than the instrument's energy range (~40 eV). As shown in Figure 5e, the first field-aligned suprathermal H⁺ ions observed by C3 at ~16:12 UT were at an energy of ~100 eV, suggesting polar-wind H⁺ ions being accelerated parallelly from 1 to 100 eV. If we consider that the Poynting fluxes caused a field-aligned potential of 100 eV in the region between 1,000 and 15,000 km altitude, for a 1 eV H⁺ polar wind ion already at 1,000 km, as it moves upward, it would be accelerated by this parallel electric field to 100 eV when it reaches 15,000 km altitude in about 160 s (this estimate time would be shorter if the altitude range for the 100 V potential is shorter). It would then take this 100 eV H⁺ ion another 210 s to move from 15,000 km to 6.5 R_E, thus a total of ~6 min travel time. This is significantly closer to the 8-min delay compared to the first scenario.

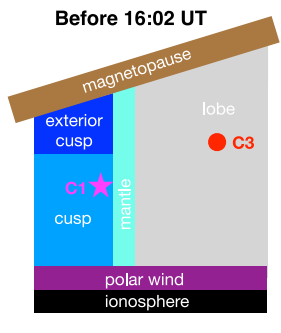
Therefore, based on the above simple estimations, we conclude that the H⁺ ion beams and conics observed by C3 in the lobe were likely a result of the pre-existing polar wind ions being accelerated by the enhanced Poynting fluxes. Note that the scenarios in Figure 9 do not require a spacecraft to remain on the same magnetic field lines to see the Poynting fluxes first and outflows later. We expect that the enhanced downward Poynting fluxes and the resulting outflows occurred over the entire polar cap, as supported by the simulation results shown in Paper 2. Thus, the scenarios apply to C3 since it remained in the lobe on the field lines connected to the polar cap.

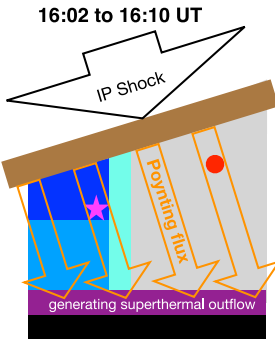
Note that the first scenario in Figure 9 might also occur in this event. Even though it cannot explain the initial appearance of the H⁺ outflow, it may explain the weak outflowing H⁺ ions observed by C3 after 16:30 UT shown in Figure 2g. Regarding acceleration of the polar wind, the parallel electric field is considered as an important

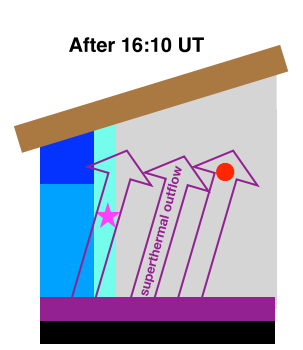
WANG ET AL. 15 of 18

21699402, 2024, 9, Downloaded from https://agupubs.onlinelibrary.wiley.com/doi/10.1029/2024JA032557 by CHIH-PING WANG - University Of California, Los

Summary of observations and relevant processes







- · Observations · Processes
- · 16:00 UT: C1 in the cusp, C3 in the lobe
- IP shock front arrived, pushed the magnetopause inward
- · 16:02 UT: YM-H jumped
- Magnetospheric magnetic fields were compressed
- 16:03-16:04 UT: C1 and C3 saw magnetic field changes
- Magnetosphere compression enhanced Poynting fluxes flowing downward from the magnetopause to the ionosphere
- 16:04 UT: Downward Poynting flux at C3 started to increase
- Poynting fluxes drove processes that accelerated pre-existing polar wind to generate superthermal outflow ions flowing upward
- The exterior cusp was pushed to lower altitude along with the inward magnetopause
- · 16:07 UT: C1 saw exterior cusp
- The cusp moved to lower latitude due to more negative IMF $\mathbf{B}_{\mathbf{z}}$
- Superthermal outflow reached C1
- 16:10 UT: C1 saw mantle and superthermal outflow
- · Superthermal outflow reached C3
- 16:12 UT: C3 saw superthermal outflow ion beam
- 16:15 UT: C3 saw superthermal outflow ion conic

Figure 10. Schematic summary of the observations and relevant processes.

mechanism for suprathermal outflows at the auroral latitudes, where FACs are enhanced by disturbances within the plasma sheet. In this event, we showed that enhancements of FACs down to the polar cap driven by an IP shock impact can also result in large H⁺ suprathermal outflows into the lobe. In addition, the appearance of ion conics suggested perpendicular acceleration by waves. Those responsible waves were likely driven by the enhanced Poynting fluxes at altitudes below 10,000 km, which explains why there were no substantial enhancements of electric field wave observed by C3.

5. Summary

In this study, we used two Cluster spacecraft, one in the cusp and one in the lobe, to analyze an event of outflowing H^+ ions in the lobe resulting from the impact of an IP shock on the magnetosphere. The key observations and the relevant processes are schematically summarized in Figure 10. By comparing the observations at the two locations, we ruled out that the appearance of the H^+ outflows in the lobe was due to encountering the cusp. The shock impact caused an increase in SYM-H. The spacecraft in the lobe at altitudes of \sim 6.5 R_E observed enhanced downward DC Poynting fluxes \sim 2 min after the SYM-H increase and then, after another 8 min, the appearance of outflowing H^+ ion beams and ion conics. Interestingly, a similar increasing trend with a time scale of \sim 5 min was seen in the increases of SYM-H, the downward DC Poynting fluxes, and the outflowing H^+ fluxes. Thus, the increasing outflow fluxes were highly correlated with the increasing downward DC Poynting fluxes with the 8-

WANG ET AL. 16 of 18

min time delay. We also examined other outflow drivers but did not find good correlations with the outflow fluxes. Based on our understanding of how Poynting fluxes affect outflow, we concluded that such time delay can be explained by the time needed for the enhanced DC Poynting fluxes to reach down to lower altitudes, drive processes to accelerate pre-existing polar wind ions to ion beams and ion conics, and then these suprathermal ions flow upward to the spacecraft altitudes. This conclusion is also supported by the simulation results presented in Paper 2.

Data Availability Statement

The Cluster data are available on the Cluster Science Archive website (https://csa.esac.esa.int). The solar wind and IMF parameters and PC(N) index are available on NASA CDAWeb (http://cdaweb.gsfc.nasa.gov/cdaweb/istp_public/). The SYM-H index from Word Data Center for Geomagnetism, Kyoto and the PC(N) index from National Space Institute (DTU Space), Technical University of Denmark are available on NASA CDAWeb (http://cdaweb.gsfc.nasa.gov/cdaweb/istp_public/).

Acknowledgments References

We thank the NASA LWS Cold Plasma team for constructive discussion. C.-P. Wang is supported by NASA 80NSSC22K1012 and NSF-GEM 2224108. Xuevi Wang and Yu Lin are supported by NASA 80NSSC22K1012 and NSF-GEM 2224109. We thank Cluster Science Archive for providing an open access to the Cluster data for free. We thank J. H. King, N. Papatashvilli at AdnetSystems, NASA Goddard Space Flight Center and CDAWeb for providing an open access to the OMNI data for free. We acknowledge Word Data Center for Geomagnetism, Kyoto for providing an open access to the SYM-H index for free.

- André, M., Crew, G. B., Peterson, W. K., Persoon, A. M., & Pollock, C. J. (1990). Ion heating by broadband low-frequency waves in the cusp/cleft. *Journal of Geophysical Research*, 95, 20809–20823. https://doi.org/10.1029/JA095iA12p20809
- Balogh, A., Dunlop, M. W., Cowley, S. W. H., Southwood, D. J., Thomlinson, J. G., Glassmeier, K. H., et al. (1997). The cluster magnetic field investigation. *Space Science Reviews*, 79(1/2), 65–91. https://doi.org/10.1023/A:1004970907748
- Chang, T., & Coppi, B. (1981). Lower hybrid acceleration and ion evolution in the suprauroral region. *Geophysical Research Letters*, 8(12), 1253–1256. https://doi.org/10.1029/GL008i012p01253
- Chang, T., Crew, G. B., Hershkowitz, N., Jasperse, J. R., Retterer, J. M., & Winningham, J. D. (1986). Transverse acceleration of oxygen ions by electromagnetic ion cyclotron resonance with broadband left-hand polarized waves. *Geophysical Research Letters*, 13(7), 636–639. https://doi.org/10.1029/GL013i007p00636
- Chappell, C. R., Giles, B. L., Moore, T. E., Delcourt, D. C., Craven, P. D., & Chandler, M. O. (2000). The adequacy of the ionospheric source in supplying magnetospheric plasma. *Journal of Atmospheric and Solar-Terrestrial Physics*, 62(6), 421–436. https://doi.org/10.1016/S1364-6826
- Chappell, C. R., Moore, T. E., & Waite, J. H., Jr. (1987). The ionosphere as a fully adequate source of plasma for the Earth's magnetosphere.
- Chaston, C. C., Bonnell, J. W., Carlson, C. W., McFadden, J. P., Ergun, R. E., Strangeway, R. J., & Lund, E. J. (2004). Auroral ion acceleration in dispersive Alfvén waves. *Journal of Geophysical Research*, 109(A4), A04205. https://doi.org/10.1029/2003JA010053
- Cornilleau-Wehrlin, N., Chanteur, G., Perraut, S., Rezeau, L., Robert, P., Roux, A., et al. (2003). First results obtained by the Cluster STAFF experiment. Annales Geophysicae, 21(2), 437–456. https://doi.org/10.5194/angeo-21-437-2003
- Crew, G. B., Chang, T., Retterer, J. M., Peterson, W. K., Gurnett, D. A., & Huff, R. L. (1990). Ion cyclotron resonance heated conics—Theory and observations. *Journal of Geophysical Research*, 95(A4), 3959. https://doi.org/10.1029/ja095ia04p03959
- Endo, M., Fujii, R., Ogawa, Y., Buchert, S., Nozawa, S., Watanabe, S., & Yoshida, N. (2000). Ion upflow and downflow at the topside ionosphere observed by the EISCAT VHF radar. *Annales de Geophysique*, 18(2), 170–181. https://doi.org/10.1007/s00585-000-0170-3
- Ergun, R. E., Andersson, L., Main, D., Su, Y.-J., Newman, D. L., Goldman, M. V., et al. (2004). Auroral particle acceleration by strong double layers: The upward current region. *Journal of Geophysical Research*, 109(A12), A12220, https://doi.org/10.1029/2004JA010545
- Escoubet, C. P., Schmidt, R., & Goldstein, M. L. (1997). Cluster—Science and mission overview. Space Science Reviews, 79(1/2), 11–32. https://doi.org/10.1023/A:1004923124586
- Horwitz, J. L., Baugher, C. R., Chappell, C. R., Shelley, E. G., & Young, D. T. (1982). Conical pitch angle distributions of very low-energy ion fluxes observed by ISEE 1. *Journal of Geophysical Research*, 87(A4), 2311–2320. https://doi.org/10.1029/JA087iA04p02311
- Johnstone, A. D., Alsop, C., Burge, S., Carter, P. J., Coates, A. J., Coker, A. J., et al. (1997). PEACE: A plasma electron and current experiment. Space Science Reviews, 79(1/2), 351–398. https://doi.org/10.1023/A:1004938001388
- Kistler, L. M., Asamura, K., Kasahara, S., Miyoshi, Y., Mouikis, C. G., Keika, K., et al. (2023). The variable source of the plasma sheet during a geomagnetic storm. *Nature Communications*, 14(1), 6143. https://doi.org/10.1038/s41467-023-41735-3
- Kistler, L. M., Mouikis, C. G., Klecker, B., & Dandouras, I. (2010). Cusp as a source for oxygen in the plasma sheet during geomagnetic storms. Journal of Geophysical Research, 115(A3), A03209. https://doi.org/10.1029/2009JA014838
- Lavraud, B., Fedorov, A., Budnik, E., Grigoriev, A., Cargill, P. J., Dunlop, M. W., et al. (2004). Cluster survey of the high-altitude cusp properties:
- A 3 yr statistical study. Annales Geophysicae, 22(8), 3009–3019. https://doi.org/10.5194/angeo-22-3009-2004

 Lavraud, B., Fedorov, A., Budnik, E., Thomsen, M. F., Grigoriev, A., Cargill, P. J., et al. (2005). High-altitude cusp flow dependence on IMF orientation: A 3 yr cluster statistical study. Journal of Geophysical Research, 110(A2), A02209. https://doi.org/10.1029/2004JA010804
- Lu, G., Reiff, P. H., Moore, T. E., & Heelis, R. A. (1992). Upflowing ionospheric ions in the auroral region. *Journal of Geophysical Research*, 97(A11), 16855–16863. https://doi.org/10.1029/92JA01435
- Moore, T. E., & Horwitz, J. L. (2007). Stellar ablation of planetary atmospheres. Reviews of Geophysics, 45(3), RG3002. https://doi.org/10.1029/2005RG000194
- Moore, T. E., Peterson, W. K., Russell, C. T., Chandler, M. O., Collier, M. R., Collin, H. L., et al. (1999). Ionospheric mass ejection in response to a CME. *Geophysical Research Letters*, 15, 2339–2342. https://doi.org/10.1029/1999gl900456
- a CME. Geophysical Research Letters, 15, 2339–2342. https://doi.org/10.1029/1999gi900456

 Mouikis, C. G., Kistler, L. M., Liu, Y. H., Klecker, B., Korth, A., & Dandouras, I. (2010). H+ and O+ content of the plasma sheet at 15–19 Re as a function of geomagnetic and solar activity. Journal of Geophysical Research, 115(A12), A00J16. https://doi.org/10.1029/2010JA015978
- Papitashvili, N. E., & King, J. H. (2020). "OMNI 1-min Data" solar wind parameters and IMF. NASA Space Physics Data Facility. https://doi.org/10.48322/45bb-8792
- Paschmann, G., Melzner, F., Frenzel, R., Vaith, H., Parigger, P., Pagel, U., et al. (1997). The electron drift instrument for Cluster. Space Science Reviews, 79, 233–269. https://doi.org/10.1007/978-94-011-5666-0_10

WANG ET AL. 17 of 18



Journal of Geophysical Research: Space Physics

- 10.1029/2024JA032557
- Peterson, W. K., Andersson, L., Callahan, B. C., Collin, H. L., Scudder, J. D., & Yau, A. W. (2008). Solar-minimum quiet time ion energization and outflow in dynamic boundary related coordinates. *Journal of Geophysical Research*, 113(A7), A07222. https://doi.org/10.1029/20081A013059
- Reiff, P. H., Lu, G., Burch, J. L., Winningham, J. D., Frank, L. A., Craven, J. D., et al. (1993). On the high- and low-altitude limits of the auroral electric field region. In R. L. Lysak (Ed.). Auroral plasma dynamics. https://doi.org/10.1029/GM080p0143
- Rème, H., Aoustin, C., Bosqued, J. M., Dandouras, I., Lavraud, B., Sauvaud, J. A., et al. (2001). First multispacecraft ion measurements in and near the Earth's magnetosphere with the identical CLUSTER Ion Spectrometry (CIS) experiment. *Annales Geophysicae*, 19(10/12), 1303–1354. https://doi.org/10.5194/angeo-19-1303-2001
- Sharp, R. D., Johnson, R. G., & Shelley, E. G. (1977). Observation of an ionospheric acceleration mechanism producing energetic (keV) ions primarily normal to the geomagnetic field direction. *Journal of Geophysical Research*, 82(22), 3324–3328. https://doi.org/10.1029/
- Strangeway, R. J., Ergun, R. E., Su, Y.-J., Carlson, C. W., & Elphic, R. C. (2005). Factors controlling ionospheric outflows as observed at intermediate altitude. *Journal of Geophysical Research*, 110(A3), A03221. https://doi.org/10.1029/2004JA010829
- Strangeway, R. J., Russell, C. T., Carlson, C. W., McFadden, J. P., Ergun, R. E., Temerin, M., et al. (2000). Cusp field-aligned currents and ion outflows. *Journal of Geophysical Research*, 105(A9), 21129–21142. https://doi.org/10.1029/2000ja900032
- Su, Y.-J., Horwitz, J. L., Moore, T. E., Giles, B. L., Chandler, M. O., Craven, P. D., et al. (1998). Polar wind survey with the thermal ion dynamics experiment/plasma source instrument suite aboard POLAR. *Journal of Geophysical Research*, 103(A12), 29305–29337. https://doi.org/10.1029/98IA02662
- Su, Y.-J., Horwitz, J. L., Wilson, G. R., Richards, P. G., Brown, D. G., & Ho, C. W. (1998). Self-consistent simulation of the photoelectron-driven polar wind from 120 km to 9 R_F altitude. *Journal of Geophysical Research*, 103(A2), 2279–2296. https://doi.org/10.1029/97JA03085
- Tsyganenko, N. A. (1995). Modeling the Earth's magnetospheric magnetic field confined within a realistic magnetopause. *Journal of Geophysical Research*, 100(A4), 5599–5612. https://doi.org/10.1029/94ja03193
- Tsyganenko, N. A. (1996). Effects of the solar wind conditions on the global magnetospheric configuration as deduced from data-based field models. In *Proceedings of the ICS-3 conference on substorms* (Vol. 389, pp. 181–185). European Space Agency.
- Wang, C.-P., Wang, X., Lin, Y., Mouikis, C. G., & Masson, A. (2024). Suprathermal outflowing H⁺ ions in the lobe driven by an interplanetary shock: 2. A 3D global hybrid simulation. *Journal of Geophysical Research*, the companion paper to this paper.
- Wanliss, J. A., & Showalter, K. M. (2006). High-resolution global storm index: Dst versus SYM-H. Journal of Geophysical Research, 111(A2), A02202. https://doi.org/10.1029/2005JA011034
- World Data Center For Geomagnetism, Copenhagen. (2019). The Polar Cap North (PCN) index (definitive) [Dataset]. DTU Space, Geomagnetism. https://doi.org/10.11581/DTU:00000057
- Yau, A., Peterson, W., & Abe, T. (2011). Influences of the ionosphere, thermosphere and magnetosphere on ion outflows. https://doi.org/10.1007/978-94-007-0501-2_16
- Yau, A. W., Takumi, A., & Peterson, W. K. (2007). The polar wind: Recent observations. *Journal of Atmospheric and Solar-Terrestrial Physics*, 69(16), 1936–1983. https://doi.org/10.1016/j.jastp.2007.08.010
- Zhao, K., Kistler, L. M., Lund, E. J., Nowrouzi, N., Kitamura, N., & Strangeway, R. J. (2020). Factors controlling O⁺ and H⁺ outflow in the cusp during a geomagnetic storm: FAST/TEAMS observations. *Geophysical Research Letters*, 46(11), e2020GL086975. https://doi.org/10.1029/2020GL086975

WANG ET AL. 18 of 18